



Cite this: *RSC Adv.*, 2024, 14, 8790

# The role of solution temperature in characteristics of TiO<sub>2</sub> nanotube arrays prepared on Ti foil in acid solution

Wenhao Xian,  Yingjie Liu, Qingjie Qi,\* Han Liu, Yue Wang and Changbin Chen

The characteristics of TiO<sub>2</sub> nanotube arrays (TNTs) prepared on Ti foil in sulfuric acid solution that contains Cl<sup>−</sup> under different temperatures are investigated by field emission scanning electron microscopy (FESEM), electrochemical impedance spectroscopy (EIS), Mott–Schottky measurement and Raman spectra. The solution temperature significantly affects the morphologies of TNTs, *i.e.*, when solution temperature rises from −10 °C to 90 °C, the inner diameter of the nanotube increases and the barrier layer thickness decreases, and, as TNTs display n-type semiconductive properties, the donor density ( $N_D$ ) and corrosion protection decrease. Two types (types I and II) of pulse temperature are used to fabricate TNTs, in which type I is firstly anodized at a low temperature for time *t*, and then increases to a high temperature. While for type II, the solution temperature order is opposite to that of type I. The  $N_D$  of TNTs in the case of type I is lower than  $N_D$  of TNTs in the case of type II.  $N_D$  decreases with the increased pulse step time for type I, while  $N_D$  increases with the increased pulse step time for type II.

Received 3rd February 2024

Accepted 8th March 2024

DOI: 10.1039/d4ra00875h

rsc.li/rsc-advances

## 1. Introduction

TiO<sub>2</sub> nanotube arrays (TNTs) have attracted tremendous attention from more and more researchers since they were invented in 1999 on account of their remarkable characteristics,<sup>1</sup> such as nano-size, large specific surface area, open hollow and regular vertical structure, easy fabrication, low cost, chemical and thermal stability, and the above specific characteristics are why TNTs are used in many applications, such as dye-sensitized solar cells,<sup>2–5</sup> super-capacitors, photocatalysis,<sup>6–9</sup> sensor manufacturing,<sup>10–12</sup> drug delivery,<sup>13–17</sup> Li-ion battery materials<sup>18–21</sup> and treatment of diseases.<sup>22,23</sup> In the past, electrochemical anodization,<sup>24,25</sup> electrochemical lithography,<sup>26</sup> photoelectrochemical etching,<sup>27</sup> sol–gel processing,<sup>28</sup> hydrothermal synthesis,<sup>29</sup> template synthesis<sup>30,31</sup> and the combination of techniques from electrochemical anodization and photolithography included,<sup>32</sup> were used to fabricate TNTs. Among them, electrochemical anodization is deemed as the most feasible method for its controllable nanotubular structures have almost perfect vertical alignment.<sup>33</sup> The so-called electrochemical method refers to exerting a DC voltage betwixt the anode (Ti foil) and the cathode (the equivalent area Pt foil) in the solution containing fluoride ions, and TiO<sub>2</sub> passive film initially formed on Ti foil in the air will dissolve under the attack of fluoride ions before TNTs. Thus, the fabrication of TNTs is a balance between electrochemical anodization and chemical dissolution, in which electrochemical

anodization promotes the formation of TiO<sub>2</sub> film on Ti foil, and chemical dissolution refers to the dissolution of TiO<sub>2</sub> film under attack from the F<sup>−</sup> ions in the electrolyte. The influences of some dominant factors such as DC voltage, fluoride ions, electrolyte and the substrate, water content, *etc.*, on the characteristics of TNTs, have been widely studied in the previous reports.<sup>22,34–39</sup> Through these reports we can infer that any process or factor which affects the electrochemical oxidation or chemical dissolution of Ti foil influences electrochemical anodization and chemical dissolution of TNTs at the same time, and consequently affects the morphologies of TNTs. However, another important factor is electrolyte temperature, and we can know that few papers systematically focus on this parameter, which can significantly affect the oxidation and dissolution rate of TiO<sub>2</sub> passive film, and thus has the potential to affect the characteristics of TNTs.<sup>40–42</sup> Therefore, this paper aims to study how the electrolyte temperature influence the morphologies and characteristics of TNTs in sulfuric acid solution.

## 2. Experiment details

### 2.1 Preparation of TiO<sub>2</sub> nanotube arrays

The thickness of Ti foil (10 × 10 mm) is 0.1 mm, which was provided by Baoji Haiji Titanium Co., Ltd. The two-electrode system is adopted to prepare TNTs at 20 V for 2 hours in the H<sub>2</sub>SO<sub>4</sub> solution that contains 0.15 M HF solution at different temperatures with a DC power supply (Itech 6874A). Ti foil is the anode while the Pt foil with the same area is the cathode. The solution is constantly stirred by a magnetic stirrer across the anodization process. Then, samples are fully washed by

Emergency Science Research Institute, China Coal Research Institute, Beijing, China



deionized water, and heated at 550 °C in air for three hours, in order to improve the crystallinity of the TNTs.<sup>43,44</sup> The temperature increases and decreases at 2.5 °C min<sup>-1</sup> to promote crystallinity.<sup>45</sup> The Mott–Schottky curves of TNTs are measured in a 0.5 M Na<sub>2</sub>SO<sub>4</sub> solution.

## 2.2 Electrochemical tests and characterizations

A Solatron 1260+1287 Electrochemical Workstation was used for electrochemical studies. The electrochemical studies were performed using a conventional three-electrode system. A Pt foil is the counter electrode and a saturated calomel electrode (SCE) is the reference electrode.

EIS are carried out at the open circuit potential (OCP) with a 10 mV potential amplitude from 10 kHz to 5 mHz. The results are fitted by ZSimpWin.

Mott–Schottky curves are tested from −0.6 V<sub>SCE</sub> to 1.0 V<sub>SCE</sub> with a scan rate of 10 mV S<sup>-1</sup>.

Micro-Raman spectra are tested with a Horiba Jobin HR800 Raman spectrometer (15 mW, 514 nm) and the resolution is 0.6 cm<sup>-1</sup> per pixel.

Surface and cross-sectional morphologies are characterized by a SUPRA55 Field Emission Scanning Electron Microscope (FESEM). The magnification is selected from 2000 to 4000 times, the electric field accelerating voltage is up to 30 kV, and the vacuum cavity pressure is less than 10<sup>-3</sup> Pa.

## 2.3 Mott–Schottky results

A Mott–Schottky analysis is generally used to depict the relationship between the space charge layer capacitance ( $C_{sc}$ ) and the applied potential. For an n-type semiconductor,<sup>46,47</sup>

$$C^{-2} = \frac{2}{\epsilon\epsilon_0 e N_D} \left( E - E_{FB} - \frac{KT}{e} \right), \quad (1)$$

where  $e$  is the electron charge ( $1.602 \times 10^{-19}$  C),  $N_D$  is the donor density,  $\epsilon$  is the dielectric constant of the passive film ( $\epsilon = 31$  in

this paper),<sup>48</sup>  $\epsilon_0$  is the vacuum permittivity ( $8.854 \times 10^{-14}$  F cm<sup>-1</sup>),  $K$  is the Boltzmann constant ( $1.38 \times 10^{-23}$  J K<sup>-1</sup>),  $T$  is the absolute temperature, and  $E_{FB}$  is the flat band potential. The term  $KT/e$  is commonly ignored since  $KT/e$  is only about 25 mV.

# 3. Results and discussions

## 3.1 FESEM and electronic properties of TNTs fabricated on Ti foil

Fig. 1 shows how the solution temperature affects the front morphologies of TNTs. When the solution temperature increases, the inner diameter of TNTs increases, and the distances between TNTs enlarge as well. The reason for this phenomenon is that the increase in temperature accelerates the breaking of Ti–O–Ti bonds in nanoparticles and growth of layered nanosheets.<sup>49</sup> Fig. 2a–e list the corresponded cross-sectional morphologies of TNTs fabricated at different temperatures. It was found that TNTs exhibit the bilayer structure, that is, the upper nanotube arrays and the below barrier layer. When the solution temperature goes up, the mean length of TNTs and the mean length of the barrier layer (showed in Fig. 2f) decrease significantly.

Nyquist plots and Mott–Schottky curves of TNTs prepared on Ti at 20 V for two hours in 0.15 M HF + 1.0 M H<sub>2</sub>SO<sub>4</sub> solution are tested in 0.5 M Na<sub>2</sub>SO<sub>4</sub> solution to study how temperature affects electronic characteristic of TNTs. Fig. 3a displays the Nyquist plots, which are consisted of two depressed semicircles, and the diameters of the semicircles decrease when temperature goes up, which means the lower corrosion protection of TNTs when the solution temperature goes up. The decayed corrosion protection of TNTs is resulted from the crystallinity and the barrier layer thickness with different solution temperatures (showed in Fig. 2f and 4).

Correspondingly, Mott–Schottky plots of TNTs fabricated at various temperatures are showed in Fig. 3b, it is obvious that  $C^{-2}$  increases linearly with higher potential above *ca.* 0 V<sub>SCE</sub> and

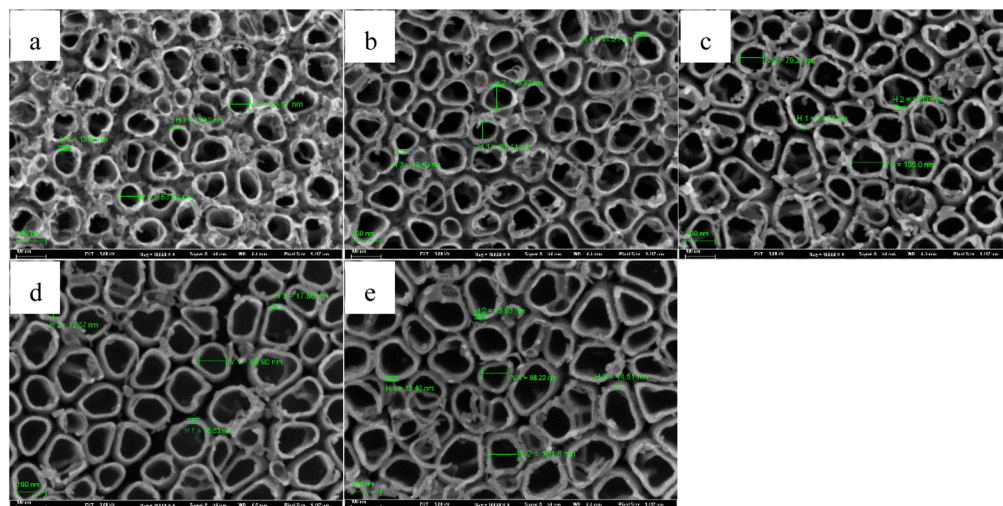


Fig. 1 Front FESEM images of TNTs prepared on Ti foil at 20 V in 0.15 M HF + 1.0 M H<sub>2</sub>SO<sub>4</sub> solution and at various temperatures, (a) −10 °C, (b) 0 °C, (c) 30 °C, (d) 60 °C, (e) 90 °C.



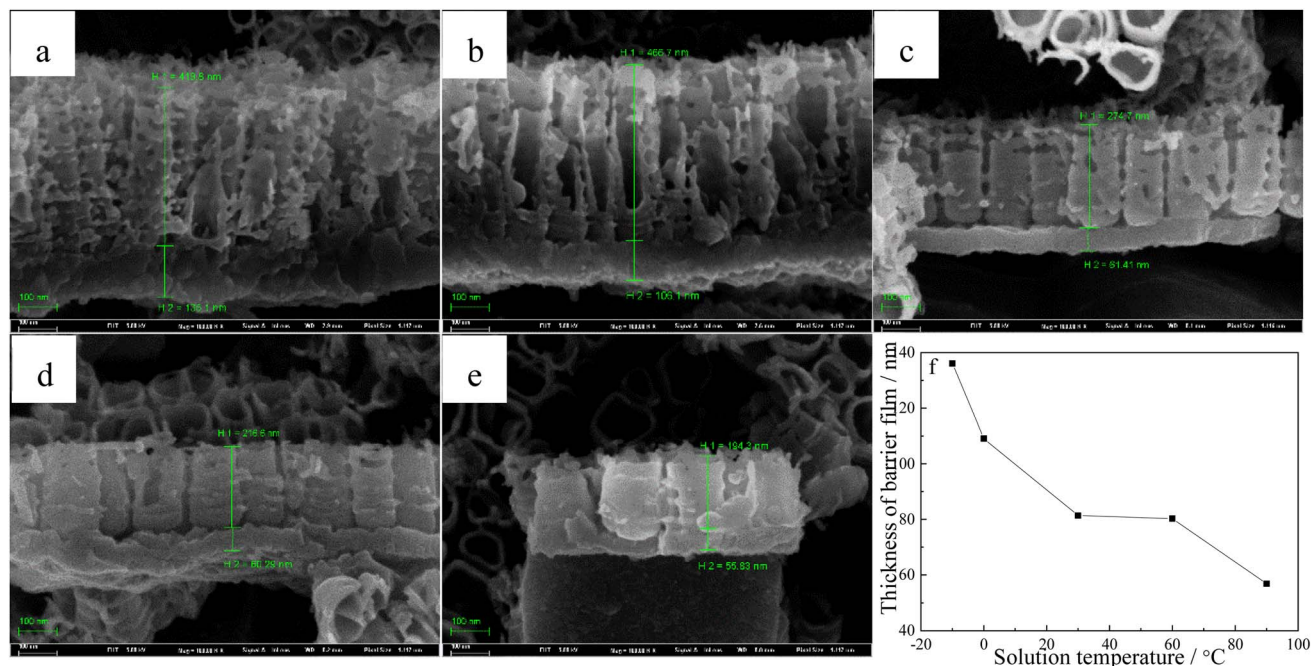


Fig. 2 Cross section FESEM images of TNTs fabricated on Ti foil at 20 V in 0.15 M HF + 1.0 M H<sub>2</sub>SO<sub>4</sub> solution and at various temperatures, (a) -10 °C, (b) 0 °C, (c) 30 °C, (d) 60 °C, (e) 90 °C, (f) thickness of the barrier film.

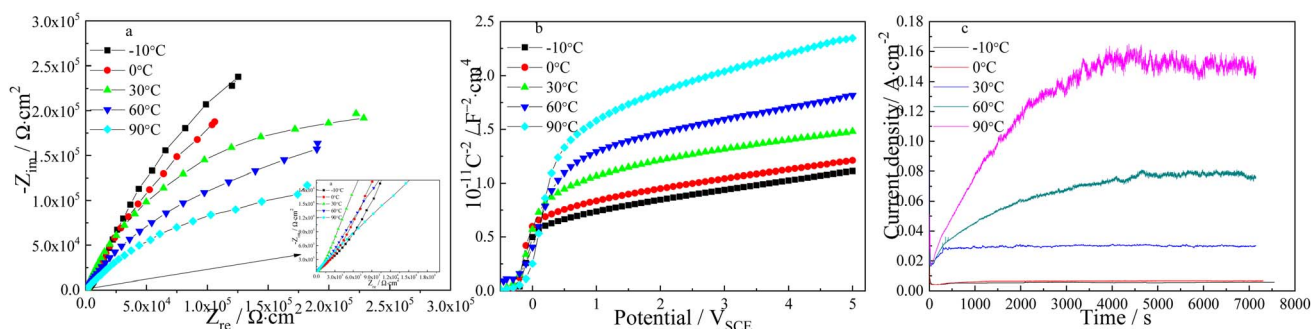


Fig. 3 Nyquist plots (a) and Mott-Schottky plots (b) measured in 0.5 M Na<sub>2</sub>SO<sub>4</sub> solution at room temperature, and the current densities verse time plots recorded during the sample preparation at 20 V in 0.15 M HF + 1 M H<sub>2</sub>SO<sub>4</sub> solution and at different temperatures (c).

$C^{-2}$  drops to the  $x$ -axis below  $ca.$  0 V<sub>SCE</sub>, which the major reasons can be surface roughness.<sup>50,51</sup> The slope of the linear region increases when solution temperature goes up, which indicates the higher  $N_D$  for the TNTs electrode. According to eqn (1), the  $N_D$  of TNTs in the case of -10 °C, 0 °C, 30 °C, 60 °C and 90 °C are calculated to be  $4.835 \times 10^{20} \text{ cm}^{-3}$ ,  $4.804 \times 10^{20} \text{ cm}^{-3}$ ,  $4.193 \times 10^{20} \text{ cm}^{-3}$ ,  $3.474 \times 10^{20} \text{ cm}^{-3}$  and  $2.741 \times 10^{20} \text{ cm}^{-3}$ , respectively. Significantly, the donor density decreases when temperature goes up. The flat-band potentials,  $E_{FB}$ , is calculated from the  $x$  intercepts of the linear region when  $C^{-2}$  equals to zero.  $E_{FB}$  in the case of -10 °C, 0 °C, 30 °C, 60 °C and 90 °C can be obtained to be -0.215 V<sub>SCE</sub>, -0.254 V<sub>SCE</sub>, -0.243 V<sub>SCE</sub>, -0.240 V<sub>SCE</sub> and -0.084 V<sub>SCE</sub> with the above method, respectively. Clearly,  $E_{FB}$  shifts to positive direction when temperature goes up, and it indicates the higher stability of TNTs.<sup>52</sup> How the temperature affects the characteristics of TNTs can be

illustrated by recording the current density during the formation process of TNTs. As displayed in Fig. 3c, the steady current density increases when temperature goes up, which implies the lower corrosion protection of TNTs.

Lower donor density and more positive  $E_{fb}$  indicate the lower corrosion susceptibility of the TNTs electrode, however, the results obtained from Fig. 3c and EIS both indicate the higher corrosion tendency of TNTs electrode with the higher solution temperature. Obviously, it is disagreement with Mott-Schottky plots. It is mainly because the barrier layer thickness of TNTs decrease when solution temperature goes up, and the barrier layer thickness is the decisive factor for its corrosion protection.<sup>41,49</sup> The composition of TNTs is studied by micro-Raman spectroscopy utilizing variable excitation wavelengths, and Fig. 4 displays 4 micro-Raman spectra of TNTs prepared by anodized Ti foil at different temperatures in 0.15 M HF + 1.0 M





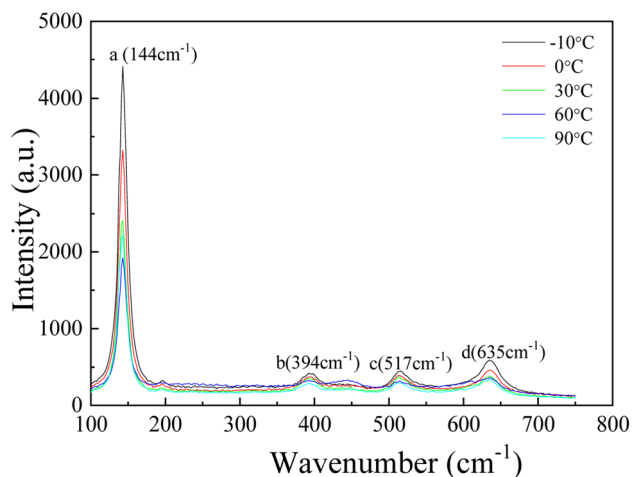


Fig. 4 Raman spectra of TNTs fabricated on Ti foil at 20 V for 2 h in 0.15 M HF + 1 M H<sub>2</sub>SO<sub>4</sub> solution and at different temperatures.

H<sub>2</sub>SO<sub>4</sub> solution. 4 Raman bands are found at 144, 394, 514 and 635 cm<sup>-1</sup>. They are assigned to 2 E<sub>g</sub> modes centered at 144 and 639 cm<sup>-1</sup>, 2 B<sub>1g</sub> modes at 399 and 519 cm<sup>-1</sup>, and 1 mode of A<sub>1g</sub> symmetry at 513 cm<sup>-1</sup> overlapping with the B<sub>1g</sub> mode at 519 cm<sup>-1</sup>. Evidently, the intensities of four peaks (peaks a, b, c and d) clearly decrease with increasing the solution temperature, indicating the decreased crystallinity of TNTs. While, the decreased crystallinity of TNTs should be consistent with the increased corrosion protection. Up to now, the results obtained from Mott–Schottky plots and Raman spectra indicate the corrosion protection of TNTs should increase with the increased solution temperature, while the results obtained from EIS and the steady current density are just reverse, hence, the major reason is only related to the decreased thickness of the barrier layer of TNTs with the increment of the solution temperature.<sup>41,42</sup>

The above results indicate that the solution temperature can significantly affect the characteristics of TNTs prepared on Ti foil in HF + H<sub>2</sub>SO<sub>4</sub> solution. It is because the variation of the growth mechanism of TNTs with different temperatures. As the formation of TNTs can be seen as balance betwixt the formation and the dissolution of the TiO<sub>2</sub> passive film, the variation of the

current density recorded during the TNTs formation showed in Fig. 3c can be divided into three stages, *i.e.*, stages I, II and III. The growth process of TNTs corresponding to the three stages is illustrated in Fig. 5, it is seen that the current density drops in stage I, which implies that the dominate process in this stage is the formation of the passive film. The growth of the passive film continues for tens of seconds in stage I, and the growth time increases when solution temperature goes down, suggesting the beneficial effect of the low solution temperature on the formation of the passive film. In stage II, it is obvious that the current density increases from the minimum to a constant density for hundreds or thousands of seconds, which means that the dominant process changes to the dissolution of the initially generated passive film, and some holes appear within the initially generated passive film. The continued time of stage II decreases and the current density grows with higher solution temperature, implying that the dissolved rate of the passive film increases and the hole size enlarges with higher temperature. While in stage III, the current density always keeps at the constant value, implying the formation and dissolution of the passive film have reached a new balance. The formed holes in stage II become regular nanotube shape, and the hole depth enlarges continuously. Furthermore, the current density in this stage increases when temperature goes up, which is consistent with the change of the barrier layer thickness at different solution temperatures.

### 3.2 Characteristics of TNTs prepared on Ti foil at 20 V under different temperature pulses in 0.15 M HF + 1.0 M H<sub>2</sub>SO<sub>4</sub>

In order to further study how solution temperature affects the characteristics of TNTs, two types of square wave pulse of the solution temperature (types I and II) are employed during the fabrication of TNTs. Fig. 6 displays the schematic of two temperature pulse, in which a lower solution temperature,  $T_1$ , is first employed during the anodization of Ti in 0.15 M HF + 1.0 M H<sub>2</sub>SO<sub>4</sub> solution at 20 V for time  $t$  and the solution temperature suddenly increases from  $T_1$  to a high temperature,  $T_2$ . After anodized for the same time at the high temperature,  $T_2$ , the solution temperature returns from the high temperature ( $T_2$ ) to the low temperature,  $T_1$ , and the rest behaviors are similar, and this temperature pulse is called type I. For type II, the solution

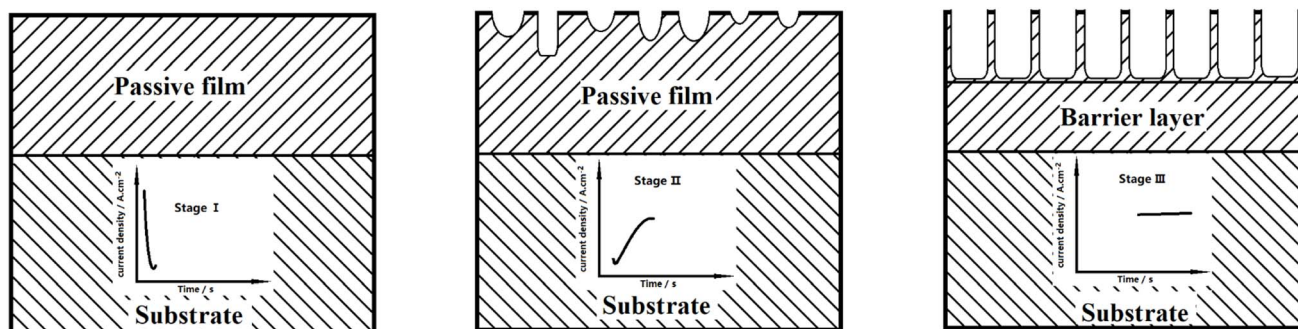


Fig. 5 The change of current density with time, recorded during the fabrication of TNTs in the case of various temperatures and the corresponding growth process of TNTs.



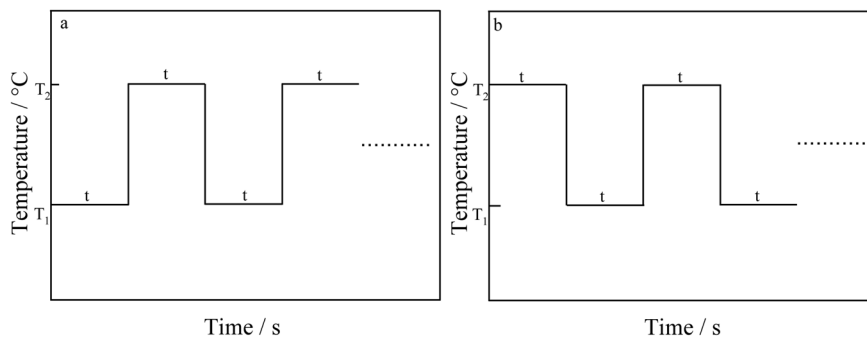


Fig. 6 Schematic of square wave temperature, (a) type I, (b) type II.

temperature order is totally opposite to type I, that is, a high solution temperature ( $T_2$ ) is employed for time  $t$ , and then, the solution temperature jumps to a low temperature,  $T_1$ , and the rest behaviors are similar (shown in Fig. 6b). It is worth mentioning that the anodization potential of Ti foil still remains at 20 V during all temperature pulse no matter using type I or type II, and the total anodization time is 2 h.

The front FESEM images of TNTs prepared on Ti foil at 20 V using the temperature pulse of type I in 0.15 M HF + 1.0 M H<sub>2</sub>SO<sub>4</sub> solution are shown in Fig. 7a–d, in which,  $T_1$  equals to 0 °C, and  $T_2$  is 60 °C, and the step anodization time is 10 min, 20 min, 30 min and 60 min, respectively. The results show that the pulse step time has little effect on the front microstructures, *i.e.*, the inner diameter of TNTs and the distances between the TNTs change little with the pulse step time. While it has an evident effect on the cross-section images, as shown in Fig. 7e–h, the mean length of nanotubes and the barrier film thickness decrease with higher pulse step time. Besides, the mean inner diameter of TNTs showed in Fig. 7a–d is clearly larger than the diameter of TNTs shown in Fig. 2b or d, indicating the TNTs prepared on Ti foil at a pulse temperature have larger inner

diameter than the TNTs prepared on Ti foil at the single temperature.

The effect of pulse step time on the corresponded Nyquist plots of TNTs is displayed in Fig. 8a, where the diameters of the depressed semicircles increase when the pulse step time goes up, and it implies the enhanced corrosion resistance of TNTs. Similarly, Fig. 8b exhibits the Mott–Schottky curves of TNTs, in which the linear region slope increases when the pulse step time goes up, and it indicates the decreased  $N_D$  for the TNTs electrode. Based on eqn (1), the  $N_D$  of TNTs in the case of 10 min, 20 min, 30 min and 60 min, are  $1.368 \times 10^{21} \text{ cm}^{-3}$ ,  $6.892 \times 10^{20} \text{ cm}^{-3}$ ,  $6.221 \times 10^{20} \text{ cm}^{-3}$  and  $5.235 \times 10^{20} \text{ cm}^{-3}$ , respectively. It is significant that  $N_D$  in the case of using type I decreases when pulse step time goes up, indicating the lower crystal degree of the TNTs. The  $E_{FB}$  in the case of 10 min, 20 min, 30 min and 60 min, can be obtained to be  $-0.421 \text{ V}_{SCE}$ ,  $-0.436 \text{ V}_{SCE}$ ,  $-0.4 \text{ V}_{SCE}$  and  $-0.464 \text{ V}_{SCE}$ , respectively. Obviously,  $E_{FB}$  shows an evident negative shift with increasing the pulse step time, indicating the lower stability of TNTs. Fig. 8c shows the corresponded micro-Raman spectra of TNTs, it is seen that the intensities of four Raman peaks evidently grow

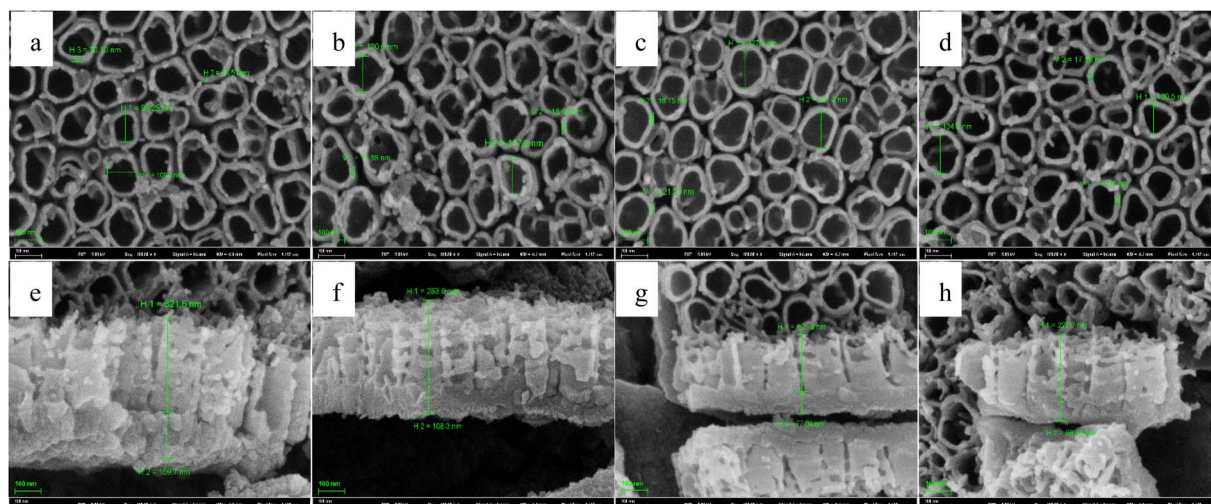


Fig. 7 Front FESEM images and the corresponding cross-section images of TNTs fabricated on Ti foil at 20 V with applying different temperature pulses in the case of type I in 0.15 M HF + 1.0 M H<sub>2</sub>SO<sub>4</sub>. (a) and (e) 10 min, (b) and (f) 20 min, (c) and (g) 30 min, (d) and (h) 60 min.



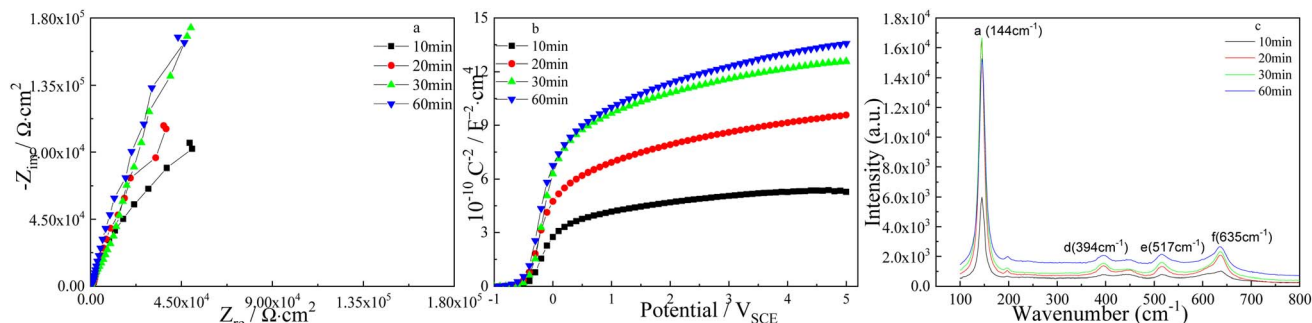


Fig. 8 Nyquist plots (a), Mott–Schottky plots (b) and Raman spectrum (c) of TNTs fabricated on Ti foil at 20 V and 25 °C with applying different temperature pulses in the case of type I in 0.15 M HF + 1.0 M H<sub>2</sub>SO<sub>4</sub> solution.

when pulse step time goes up, suggesting the enhanced crystallinity of TNTs.

For temperature pulse, the applying order of the temperature is another important parameter except the pulse step time, so we study the effect of the applying order of the solution temperature on the characteristics of TNTs. Fig. 9a–d show the front FESEM images of TNTs prepared on Ti foil at 20 V by using the type II in 0.15 M HF + 1.0 M H<sub>2</sub>SO<sub>4</sub> solution, in which,  $T_1$  equals to 60 °C, and  $T_2$  is 0 °C, and the step anodization time is 10 min, 20 min, 30 min and 60 min, respectively. Similar to Fig. 7, the pulse step time has little effect on the front microstructures in the case of using type II. While the pulse step time affects the cross-section evidently. As shown in Fig. 9e–h, the thickness of the barrier layer decreases when the pulse step time goes up.

The effect of pulse step time on the Nyquist plots of TNTs is showed in Fig. 10a, it is clear that the semicircles enlarge when the pulse step time goes up, and it implies the corrosion resistance of TNTs grows when the pulse step time goes up. However, the Mott–Schottky curves of TNTs showed in Fig. 10b

show that the linear region slope decreases with longer pulse step time, suggesting the higher  $N_D$ . According to eqn (1), the donor densities in the case of 10 min, 20 min, 30 min and 60 min, are calculated to be  $4.223 \times 10^{20} \text{ cm}^{-3}$ ,  $5.402 \times 10^{20} \text{ cm}^{-3}$ ,  $6.089 \times 10^{20} \text{ cm}^{-3}$  and  $6.355 \times 10^{20} \text{ cm}^{-3}$ , respectively. Significantly,  $N_D$  in the case of type II increases with longer pulse step time, which is converse to the donor density calculated from Fig. 8b. The flat-band potentials,  $E_{FB}$ , in the case of 10 min, 20 min, 30 min and 60 min, can be obtained to be  $-0.414 \text{ V}_{SCE}$ ,  $-0.446 \text{ V}_{SCE}$ ,  $-0.367 \text{ V}_{SCE}$  and  $-0.484 \text{ V}_{SCE}$ , respectively. Obviously,  $E_{FB}$  shows an evident negative shift with enlarging the pulse step time, suggesting the lower stability of the TNTs. Comparing the donor density extracted from Fig. 8b and 10b, it can be found that  $N_D$  obtained from Fig. 8b is always higher than that obtained from Fig. 10b at the same pulse step time, and it implies that the applying of type II is more beneficial to improve the crystal degree of TNTs than that of type I.

The composition of TNTs is studied by micro-Raman spectroscopy, and Fig. 10c displays four micro-Raman spectra of TNTs prepared by anodized Ti foil using pulse anodization of

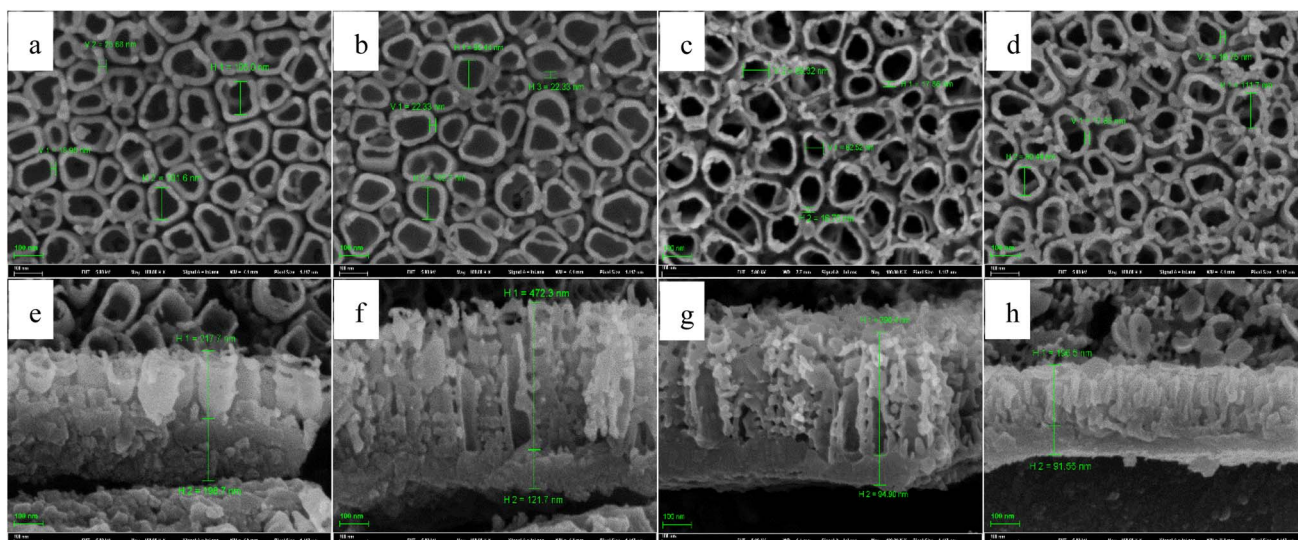


Fig. 9 Front FESEM images and the corresponding cross-section images of TNTs fabricated on Ti foil at 20 V and 25 °C with applying different temperature pulses in the case of type II in 0.15 M HF + 1.0 M H<sub>2</sub>SO<sub>4</sub>, (a) and (e) 10 min, (b) and (f) 20 min, (c) and (g) 30 min, (d) and (h) 60 min.



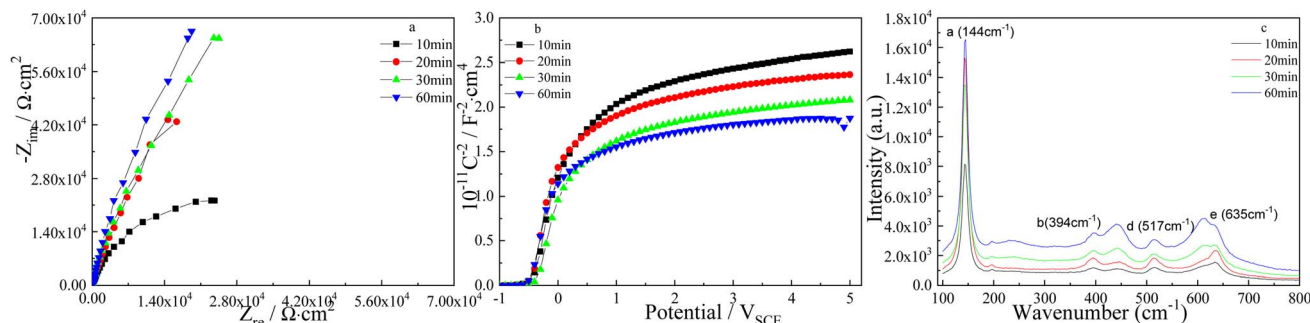


Fig. 10 Nyquist plots (a), Mott-Schottky plots (b) and Raman spectrum (c) of TNTs prepared on Ti foil at 20 V with applying various temperature pulses in the case of type II in 0.15 M HF + 1.0 M H<sub>2</sub>SO<sub>4</sub> solution.

type II. It can be observed that the intensities of four Raman peaks clearly grow when the pulse step time goes up, suggesting the better crystallinity of TNTs.

Table 1 list the influence of two temperature pulse type on the semi-conductive and microstructure parameters of TNTs, it is clear that the barrier layer thickness of TNTs fabricated whether using 0–60 °C or 60–0 °C pulse temperature pair decreases when the pulse step time goes up.  $N_D$  decreases and  $E_{FB}$  goes more negative when the pulse step time in the case of using 0–60 °C pulse temperature pair goes up. While for 60–0 °C pulse temperature pair,  $N_D$  increases and  $E_{FB}$  moves to negative direction with longer pulse step time. Meanwhile,  $N_D$  in the case of 0–60 °C pulse temperature pair (type I) at one fixed pulse step time is higher than  $N_D$  of 60–0 °C pulse temperature pair (type II) at the same pulse step time, implying the higher crystal degree of TNTs prepared on Ti foil in the case of type II. And this conclusion is verified by the Raman spectra showed in Fig. 8c and 10c as showed in above two Raman spectra, the intensity of each Raman band peak showed in Fig. 10c is always higher than that showed in Fig. 8c, meaning the higher crystallinity of TNTs fabricated using type II, and it is agreement with the conclusion obtained from Mott-Schottky plots. The difference of the microstructure and semi-conductive parameters caused by type I and type II is related to the final applied temperature during the whole fabrication. As displayed in Fig. 6, the final applied temperature in the case of type I is always the higher temperature, while the final applied temperature of type II is always the lower temperature. While Fig. 2 to 4 show that the thickness and  $N_D$  of TNTs decrease, and the crystal degree of TNTs decreases when the temperature goes up, thus, the barrier layer thickness

in the case of type I is lower than that of type II, and  $N_D$  of type II is lower than that in the case of type I.

For the insight analysis of the pulse temperature on the characteristic of TNTs, Ti foil is anodized using type I, in which, the anodization is 20 V, the total anodization time is 2 h and the solution is 0.15 M HF + 1.0 M H<sub>2</sub>SO<sub>4</sub> solution. For pulse temperature,  $T_1$  equals to 30 °C, and  $T_2$  is 55 °C, 75 °C and 95 °C, respectively. The pulse step time is 30 min. The influence of the higher pulse anodization temperature on the FESEM images of TNTs is showed in Fig. 11, it shows that the mean inner diameter of TNTs and the thickness of the barrier layer increases when the higher pulse temperature goes up. While the length of nanotube of TNTs decreases when higher pulse temperature goes up.

The effect of the higher pulse temperature on the Nyquist plots and Mott-Schottky plots of TNTs in the case of type I is displayed in Fig. 12, it is clear that the diameters of the depressed semicircles and the slope of the linear region of Mott-Schottky plots increase with the higher pulse temperature goes up, implying the higher corrosion resistance and the lower donor density of TNTs with the higher pulse temperature increases. According to eqn (1),  $N_D$  in the case of using 30–55 °C, 30–75 °C and 30–95 °C pulse temperature pair, are calculated to be  $9.191 \times 10^{20} \text{ cm}^{-3}$ ,  $7.627 \times 10^{20} \text{ cm}^{-3}$  and  $6.517 \times 10^{20} \text{ cm}^{-3}$ , respectively. Significantly,  $N_D$  decreases with the higher pulse temperature increases.  $E_{FB}$ , in the case of 30–55 °C, 30–75 °C and 30–95 °C pulse temperature pair, can be obtained to be  $-0.393 V_{SCE}$ ,  $-0.407 V_{SCE}$  and  $-0.414 V_{SCE}$ , showing a negative shift.

The influence of higher pulse temperature on the composition of TNTs is studied by micro-Raman spectroscopy, and

Table 1 Microstructure and electronic parameters of TNTs prepared on Ti foil using types I and II

Pulse step time	0–60 °C pulse temperature pair			60–0 °C pulse temperature pair		
	Thickness of barrier layer/nm	$N_D/\text{cm}^{-3}$	$E_{FB}/V_{SCE}$	Thickness of barrier layer/nm	$N_D/\text{cm}^{-3}$	$E_{FB}/V_{SCE}$
10 min	159.7	$1.368 \times 10^{21}$	−0.421	198.7	$4.223 \times 10^{20}$	−0.414
20 min	108.3	$6.892 \times 10^{20}$	−0.436	121.7	$5.402 \times 10^{20}$	−0.446
30 min	77.04	$6.221 \times 10^{20}$	−0.4	94.9	$6.088 \times 10^{20}$	−0.367
60 min	68.99	$5.235 \times 10^{20}$	−0.464	91.55	$6.355 \times 10^{20}$	−0.484



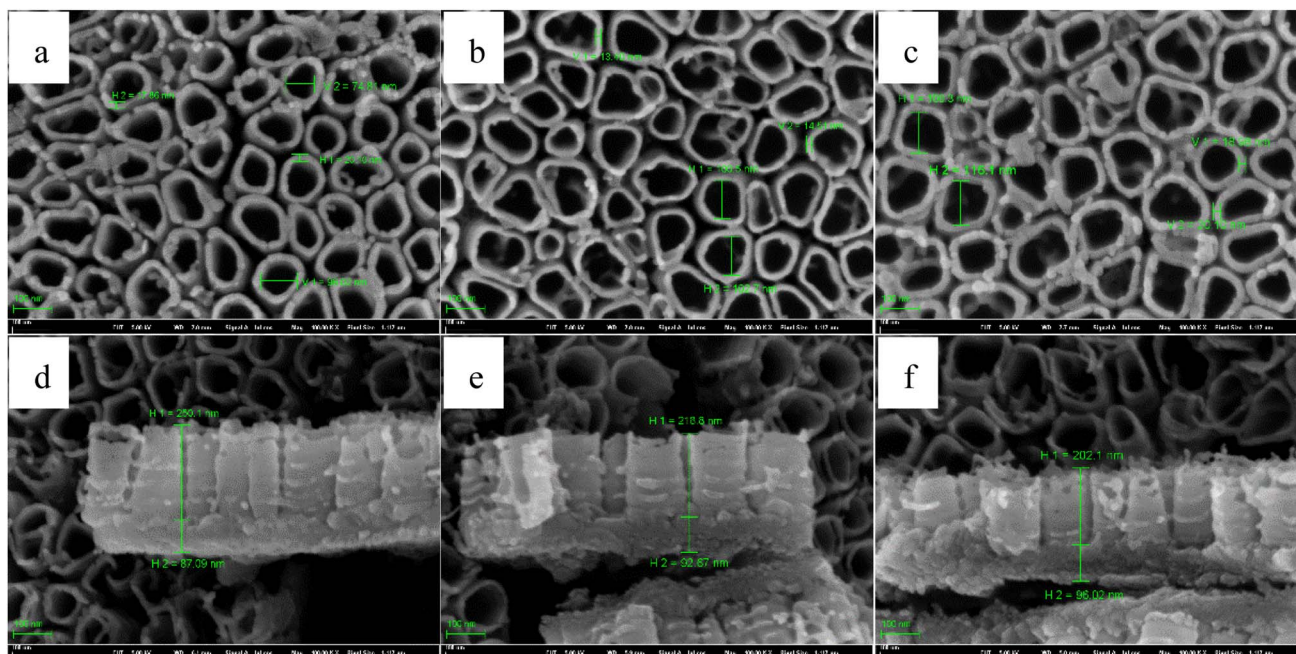


Fig. 11 Front FESEM images and the corresponding cross-section images of TNTs prepared on Ti foil at 20 V in the case of 30–55 °C (a) and (d), 30–75 °C (b) and (e) and 30–95 °C (c) and (f).

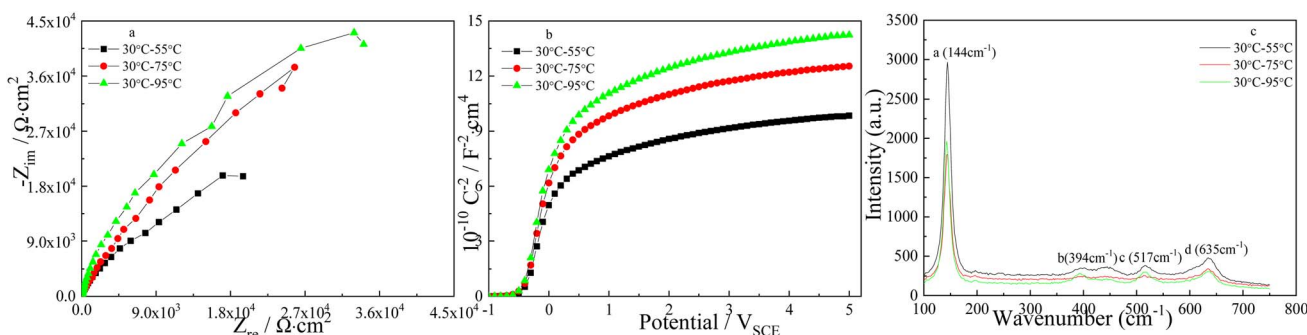


Fig. 12 Nyquist plots (a), Mott–Schottky plots (b) and Raman spectrum (c) of TNTs prepared on Ti foil at 20 V with applying different temperature pulses in the case of type I in 0.15 M HF + 1.0 M H<sub>2</sub>SO<sub>4</sub> solution.

Fig. 12c shows that the intensities of four Raman peaks significantly decrease with the higher pulse temperature increases, which implies the lower crystallinity of TNTs. While higher crystal degree of TNTs means higher corrosion susceptibility, it is consistent with the EIS and FESEM results.

Similar to Fig. 11, Fig. 13 shows the FESEM images of TNTs prepared on Ti foil using type II, in which,  $T_1$  equals to 95 °C, 75 °C and 55 °C, respectively.  $T_2$  is 30 °C, and the step anodization time is 30 min. It is clear that the higher pulse temperature affects the front microstructures of TNTs in the case of type II slightly. While the barrier layer thickness increases with the higher pulse temperature goes up, and it is resistant with Fig. 11.

The influence of the higher pulse temperature on the Nyquist plots and Mott–Schottky plots is showed in Fig. 14, it is clear that the diameters of the depressed semicircles decreases and the slope of the linear region of Mott–Schottky plots grows

when the higher pulse temperature goes up, and it implies the higher corrosion resistance and the lower  $N_D$  of TNTs. According to eqn (1),  $N_D$  in the case of using 55–30 °C, 75–30 °C and 95–30 °C pulse temperature pair, are calculated to be  $1.03 \times 10^{21} \text{ cm}^{-3}$ ,  $8.245 \times 10^{20} \text{ cm}^{-3}$  and  $7.92 \times 10^{20} \text{ cm}^{-3}$ , respectively. Obviously,  $N_D$  decreases when the higher pulse temperature goes up.  $E_{FB}$  in the case of 55–30 °C, 75–30 °C and 95–30 °C pulse temperature pair, can be obtained to be  $-0.414 \text{ V}_{SCE}$ ,  $-0.422 \text{ V}_{SCE}$  and  $-0.429 \text{ V}_{SCE}$ , respectively. Comparing  $N_D$  calculated from Fig. 12b and 14b,  $N_D$  at the fixed pulse temperatures in the case of type I is always lower than that at the fixed pulse temperatures in the case of type II, indicating the lower crystal degree of TNTs prepared on Ti foil in the case of type II.

The effect of pulse anodization temperature on the phase composition of TNTs in the case of type II is displayed in Fig. 14c, it is obvious that the feature of Raman spectra is close





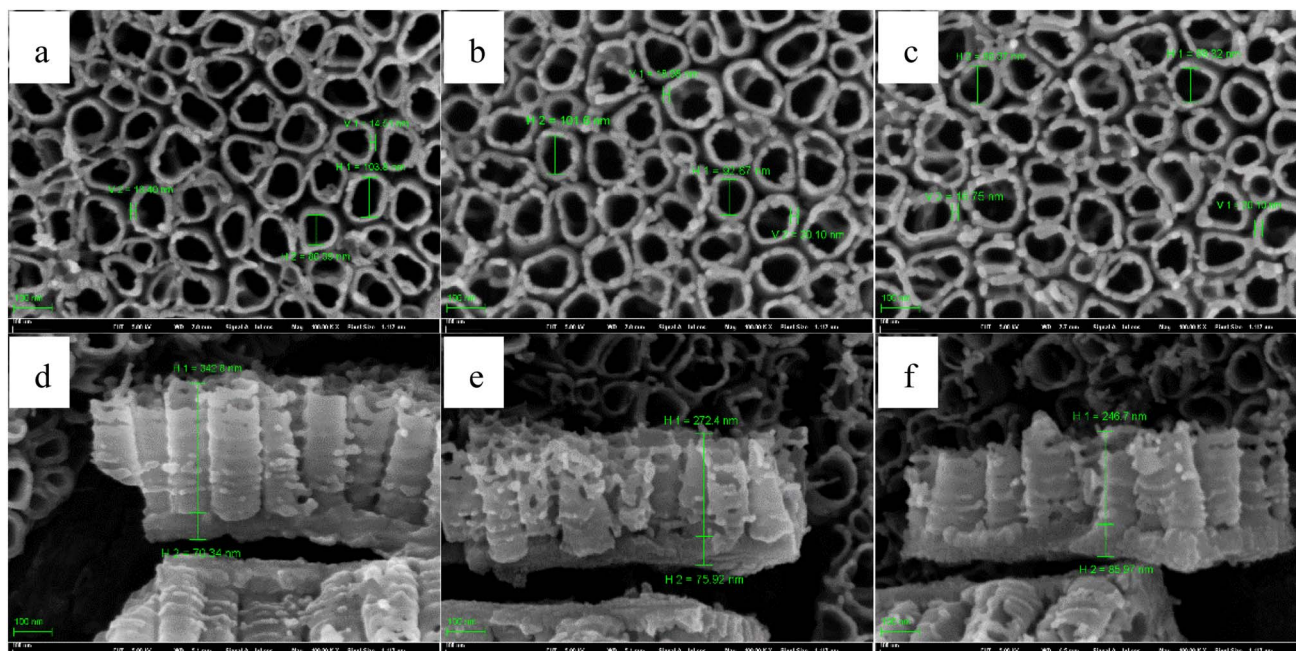


Fig. 13 Front FESEM images and the corresponding cross-section images of TNTs fabricated on Ti foil at 20 V in the case of 55–30 °C (a) and (d), 75–30 °C (b) and (e) and 95–30 °C (c) and (f).

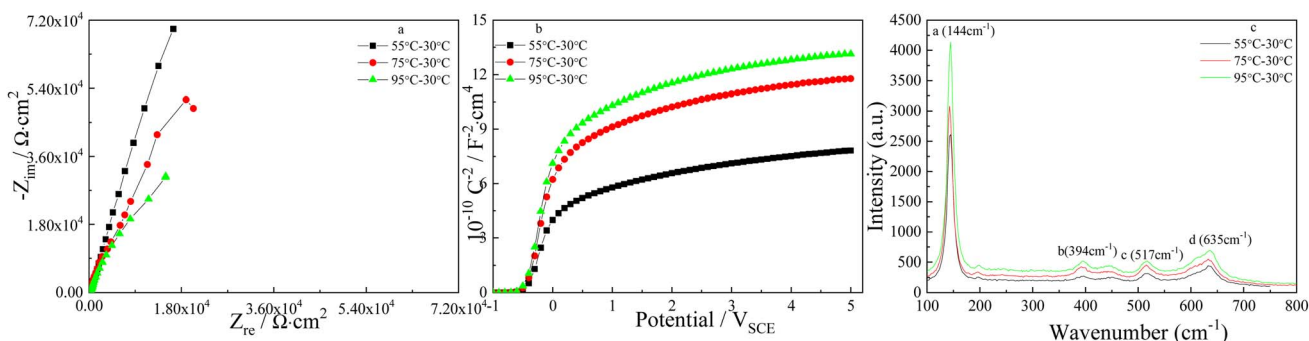


Fig. 14 Nyquist plots (a), Mott–Schottky plots (b) and Raman spectrum (c) of TNTs fabricated on Ti foil at 20 V with applying different temperature pulses in the case of type II in 0.15 M HF + 1.0 M H<sub>2</sub>SO<sub>4</sub> solution.

to the previous feature, and the intensities of four Raman peaks increase when the higher pulse temperature in the case of type II goes up, which indicates the enhanced crystallinity of TNTs, and it is reverse to the Raman spectra showed in Fig. 12c. The higher crystal degree of the TNTs means a lower diffusion resistance of the ions betwixt TNTs and the barrier films,

increasing the corrosion susceptibility, which agrees with the EIS and Mott–Schottky results.

Similar to Table 1, Table 2 lists the thickness of the barrier layer,  $N_D$  and  $E_{FB}$  of TNTs fabricated on Ti foil using the temperature pulse of type I (30–55 °C, 30–75 °C and 30–95 °C) and type II (55–30 °C, 75–30 °C and 95–30 °C). Significantly, the

Table 2 Microstructure and electronic parameters of TNTs fabricated on Ti foil using type I and II

Parameters	Type I			Type II		
	30–55 °C	30–75 °C	30–95 °C	55–30 °C	75–30 °C	95–30 °C
Thickness of barrier layer/nm	85.97	75.92	70.34	96.02	92.87	87.09
$N_D/\text{cm}^3$	$9.19 \times 10^{20}$	$7.627 \times 10^{20}$	$6.517 \times 10^{20}$	$1.03 \times 10^{21}$	$8.245 \times 10^{20}$	$7.92 \times 10^{20}$
$E_{FB}/V_{SCE}$	−0.393	−0.407	−0.414	−0.414	−0.412	−0.429



barrier layer thickness and  $N_D$  in the case of type I at the two fixed temperature pair are lower than that in the case of type II, and the reason is attributed to the final applied temperature. On the whole, TNTs fabricated on Ti foil using type I has lower thickness of the barrier layer,  $N_D$  and corrosion protection than that using type II.

## 4. Conclusions

The influences of solution temperature on the microstructure and the electronic properties of the  $\text{TiO}_2$  nanotube arrays prepared on Ti foil, are studied, from the experimental results and discussions. Some conclusions are drawn as following:

(1) The  $\text{TiO}_2$  nanotube arrays present a bilayer structure, *i.e.*, the above nanotube arrays and the below barrier layer, in which, the thickness of the barrier layer decreases when the solution temperature in the case of single temperature rises from  $-10^\circ\text{C}$  to  $90^\circ\text{C}$ . The corrosion protection and the donor density of TNTs prepared on Ti foil in  $0.15\text{ M HF} + 1.0\text{ M H}_2\text{SO}_4$  solution decrease when the solution temperature rises from  $-10^\circ\text{C}$  to  $90^\circ\text{C}$ .

(2) The pulse temperature has an evident effect on the characteristics of TNTs in the case of two fixed temperatures, *i.e.*, the barrier layer thickness and the donor density of TNTs decrease when the pulse step time rises from 10 min to 60 min, while the crystal degree and the corrosion resistant of TNTs increase in the case of type I. For type II of the pulse temperature, the barrier layer thickness of TNTs decreases, and the crystal degree, the donor density and the corrosion resistance of TNTs increase when the pulse step time rises from 10 min to 60 min.

(3) The barrier layer thickness and the corrosion resistant of TNTs increase, while the donor density and the crystal degree of TNTs decrease when the higher temperature in the case of type I rises from  $30\text{--}55^\circ\text{C}$  to  $30\text{--}95^\circ\text{C}$ . However, the barrier layer thickness and the crystal degree of TNTs increase, the corrosion resistance and the donor density of TNTs decrease when the higher temperature in the case of type II rises from  $55\text{--}30^\circ\text{C}$  to  $95\text{--}30^\circ\text{C}$ .

## Author contributions

Wenhao Xian: conceptualization and writing – original draft. Yingjie Liu: formal analysis and investigation. Qingjie Qi: funding acquisition and supervision. Han Liu: methodology. Yue Wang: writing – review & editing. Changbin Chen: investigation.

## Conflicts of interest

The authors declare that they have no conflict of interest.

## Acknowledgements

This work was supported by National Key R&D Program of China 2023YFC3011202, Project of China Coal Industry Group Co., Ltd 2022-TD-MS001 & 2022-2-MS004.

## References

- 1 V. Zwillling, M. Aucouturier and E. Darque-Ceretti, *Electrochim. Acta*, 1999, **45**, 921.
- 2 R. Hahn, T. Stergiopoulos, J. M. Macak, D. Tsoukleris, A. G. Kontos, S. P. Albu, D. Kim, A. Ghicov, J. Kunze, P. Falaras and P. Schmuki, *Phys. Status Solidi RRL*, 2007, **1**, 135.
- 3 N. F. Fahim and T. Sekino, *Chem. Mater.*, 2009, 211967.
- 4 K. I. Ishibashi, R. T. Yamaguchi, Y. Kimura and M. Niwano, *J. Electrochem. Soc.*, 2008, **155**, K10.
- 5 P. Arunachalam, M. S. Amer, H. A. AlOraij, A. M. Al-Mayouf, M. Hezam and M. Al-Shalwi, Boosting the Photoelectrochemical Water Oxidation Performance of  $\text{TiO}_2$  Nanotubes by Surface Modification Using Silver Phosphate, *Catalysts*, 2022, **12**, 11.
- 6 A. Fujishima, X. Zhang and D. A. Tryk, *Surf. Sci. Rep.*, 2008, **63**, 515.
- 7 Y. K. Lai, L. Sun and Y. C. Chen, *J. Electrochem. Soc.*, 2006, **153**, D123.
- 8 N. H. Luan and C. F. Chang, Fabrication of  $\text{Ag}_3\text{PO}_4/\text{N-doped TiO}_2$  nanotubes heterojunction photocatalysts for visible-light-driven photocatalysis, *Chemosphere*, 2024, **350**, 141022.
- 9 B. Nurulhuda, T. W. Kian, K. Go, M. Atsunori and L. Zainovia, Comparison of  $\text{ZrO}_2$ ,  $\text{TiO}_2$ , and  $\alpha\text{-Fe}_2\text{O}_3$  nanotube arrays on  $\text{Cr(VI)}$  photoreduction fabricated by anodization of Zr, Ti, and Fe foils, *Mater. Res. Express*, 2020, **7**, 055013.
- 10 I. D. Kim, A. Rothschild, B. H. Lee, D. Y. Kim, S. M. Jo and H. L. Tuller, *Nano Lett.*, 2006, **6**, 2009.
- 11 M.-H. Seo, M. Yuasa, T. Kida, J.-S. Huk, K. Shimanoe and N. Yamazoe, *Sens. Actuators, B*, 2009, **137**, 513.
- 12 B. Kumar and S. K. Sinha, Nanostructured  $\text{Cu}_2\text{O}$  deposited on  $\text{TiO}_2$  nanotube arrays for ultra-sensitive non-enzymatic glucose electrochemical biosensor, *Ionics*, 2023, **29**, 2.
- 13 N. K. Shrestha, J. M. Macak, F. Schmidt-Stein, R. Hahn, C. T. Mierke, B. Fabry and P. Schmuki, *Angew. Chem.*, 2009, **121**, 987.
- 14 N. K. Shrestha, J. M. Macak, F. Schmidt-Stein, R. Hahn, C. T. Mierke, B. Fabry and P. Schmuki, *Angew. Chem., Int. Ed.*, 2009, **48**, 969.
- 15 L. Z. Wu, X. Wu, L. Z. Wu, D. D. Chen, T. Zhang, H. Zheng and X. F. Xiao, Polydopamine-Modified Titanium Dioxide Nanotube Arrays Doped with Calcium as a Sustained Drug Delivery System, *ACS Omega*, 2024, **9**, 4.
- 16 K. Q. Tang, H. Su and Z. Qu, Preparation of honokiol-loaded titanium dioxide nanotube drug delivery system and its effect on CAL-27 cells, *Front. Bioeng. Biotech.*, 2023, **11**, 1249349.
- 17 V. Galstyan, J. M. Macak and T. Djenizian, Anodic  $\text{TiO}_2$  nanotubes: a promising material for energy conversion and storage, *Appl. Mater. Today*, 2022, **29**, 101613.
- 18 Y. C. Nah, A. Ghicov, D. Kim, S. Berger and P. Schmuki, *J. Am. Chem. Soc.*, 2008, **130**, 16154.
- 19 A. Ghicov, M. Yamamoto and P. Schmuki, *Angew. Chem.*, 2008, **120**, 8052–8055.



- 20 A. Benoit, I. Paramasivam, Y. C. Nah, P. Roy and P. Schmuki, *Electrochem. Commun.*, 2009, **11**, 728.
- 21 A. Q. Li, X. N. Han, L. H. Deng and X. Wang, Mechanical properties of tunneling nanotube and its mechanical stability in human embryonic kidney cells, *Front. Cell Dev. Biol.*, 2022, **10**, 955676.
- 22 T. Saha, C. Dash, R. Jayabalan, S. Khiste, A. Kulkarni, K. Kurmi, *et al.*, Intercellular nanotubes mediate mitochondrial trafficking between cancer and immune cells, *Nat. Nanotechnol.*, 2022, **17**, 98–106.
- 23 C. Aiempnanakit, P. Junbang, W. Suphap and K. Aiempnanakit, Influence of water content on structural and electrochromic properties of TiO<sub>2</sub> nanotube prepared by anodization, *J. Met., Mater. Miner.*, 2023, **33**, 3.
- 24 D. Regonini, C. R. Bowen, A. Jaroenworarluck and R. Stevens, *Mater. Sci. Eng., R*, 2013, **74**, 377.
- 25 S. Z. Chu, S. Inoue, K. Wada, S. Hishita and K. Kurashima, *J. Electrochem. Soc.*, 2005, **152**, B116.
- 26 H. Masuda, K. Kanezawa, M. Nakao, A. Yokoo, T. Tamamura, T. Sugiura, H. Minoura and K. Nishio, *Adv. Mater.*, 2003, **15**, 159.
- 27 J. E. G. J. Wijnhoven and W. L. Vos, *Science*, 1998, **281**, 802.
- 28 W. Z. Wang, O. K. Varghese, M. Paulose, C. A. Grimes, Q. L. Wang and E. C. Dickey, *J. Mater. Res.*, 2004, **19**, 417.
- 29 P. Hoyer, *Langmuir*, 1996, **12**, 1411.
- 30 Y. S. Chen, J. C. Crittenden, S. Hackney, L. Sutter and D. W. Hand, *Environ. Sci. Technol.*, 2005, **39**, 1201.
- 31 V. Vega, J. M. Montero-Moreno, J. García, V. M. Prida, W. Rahimi, M. Waleczek, C. Bae, R. Zierold and K. Nielsch, *Electrochim. Acta*, 2016, **203**, 51.
- 32 G. K. Mor, O. K. Varghese, M. Paulose, K. Shankar and C. A. Grimes, *Sol. Energy Mater. Sol. Cells*, 2006, **90**, 2011.
- 33 J. M. Macak, H. Tsuchiya and P. Schmuki, *Angew. Chem., Int. Ed.*, 2005, **44**, 2100.
- 34 K. Yasuda and P. Schmuki, *Electrochim. Acta*, 2007, **52**, 4053.
- 35 K. Yasuda, J. Macak, S. Berger, A. Ghicov and P. Schmuki, *J. Electrochem. Soc.*, 2007, **154**, C472.
- 36 R. Beranek, H. Hilderbrand and P. Schmuki, *Electrochem. Solid-State Lett.*, 2003, **6**, B12.
- 37 J. M. Macak, H. Tsuchiya, L. Taveira, S. D. Aldabergenova and P. Schmuki, *Angew. Chem.*, 2005, **117**, 7629.
- 38 A. Ghicov, S. Aldabergenova, H. Tsuchiya and P. Schmuki, *Angew. Chem.*, 2006, **118**, 7150–7153.
- 39 J. Wang and Z. Q. Lin, *J. Phys. Chem. C*, 2009, **113**, 4026–4030.
- 40 G. K. Mor, K. Shankar, M. Paulose, O. K. Varghese and C. A. Grimes, Use of Highly-Ordered TiO<sub>2</sub> Nanotube Arrays in Dye-Sensitized Solar Cells, *Nano Lett.*, 2006, **6**, 215.
- 41 J. J. Ma, J. Xu, S. Y. Jiang, P. Munroe and Z. H. Xie, Effects of pH value and temperature on the corrosion behavior of a Ta<sub>2</sub>N nanoceramic coating in simulated polymer electrolyte membrane fuel cell environment, *Ceram. Int.*, 2016, **42**, 15.
- 42 Y. Ku, P. Y. Lin, Y. C. Liu and H. C. Wu, Fabrication of TiO<sub>2</sub> nanotube arrays of different dimension for photocatalytic decomposition of IPA in air streams, *J. Chin. Inst. Eng.*, 2017, **40**, 8.
- 43 F. Jiang, Z. Zheng, S. Zheng, Z. Xu and L. An, Effects of calcination temperatures on the structure and adsorption behavior of titaniana nanotube, *Environ. Chem.*, 2008, **27**(6), 731–735.
- 44 M. H. Suhag, I. Tateishi, M. Furukawa, H. Katsumata, A. Khatun and S. Kaneco, Application of Rh/TiO<sub>2</sub> Nanotube Array in Photocatalytic Hydrogen Production from Formic Acid Solution, *J. Compos. Sci.*, 2022, **6**(11), 327.
- 45 G. K. Mor, K. Shankar, M. Paulose, O. K. Varghese and C. A. Grimes, Use of Highly-Ordered TiO<sub>2</sub> Nanotube Arrays in Dye-Sensitized Solar Cells, *Nano Lett.*, 2006, **6**, 215.
- 46 S. R. Morrison, *Electrochemistry at Semiconductor and Oxidized Electrodes*, Plenum Press, New York, 1980.
- 47 G. Nogami, Characterization of Semiconductor Electrodes with a Deep Impurity Level, *J. Electrochem. Soc.*, 1982, **129**, 2219.
- 48 H. Tang, K. Prasad, R. Sanjinès, P. E. Schmid and F. Lévy, Electrical and optical properties of TiO<sub>2</sub> anatase thin films, *J. Appl. Phys.*, 1994, **75**, 2042.
- 49 G. B. Li, C. Z. Song, J. L. Zhang and S. Y. Tian, Formation and Photo-degradation Performance of Titania Nanotubes, *Appl. Mech. Mater.*, 2014, **665**, 284–287.
- 50 M. Tomkiewicz, *J. Electrochem. Soc.*, 1979, **126**, 1505.
- 51 H. O. Finklea, *J. Electrochem. Soc.*, 1982, **129**, 2003.
- 52 T. Ohsaka, F. Izumi and Y. Fujiki, Raman Spectrum of Anatase, TiO<sub>2</sub>, *J. Raman Spectrosc.*, 1978, **7**, 321.

